

# High resolution MCP-PMT Readout Using Transmission Lines

M. Follin<sup>a</sup>, R. Chyzh<sup>a</sup>, C.-H. Sung<sup>a</sup>, D. Breton<sup>c</sup>, J. Maalmi<sup>c</sup>, T. Chaminade<sup>a</sup>, E. Delagnes<sup>a</sup>, K. Schäfers<sup>e</sup>,  
C. Weinheimer<sup>d</sup>, D. Yvon<sup>a,b</sup>, V. Sharyy<sup>a,b,\*</sup>

<sup>a</sup>IRFU, CEA, Université Paris-Saclay, Gif-sur-Yvette, France

<sup>b</sup>BioMAPs, Service Hospitalier Frédéric Joliot, CEA, CNRS, Inserm, Université Paris-Saclay, Orsay, France

<sup>c</sup>IJCLab, IN2P3, CNRS, Université Paris-Saclay, Orsay, France

<sup>d</sup>Nuclear Physics Institute, University of Münster, Münster, Germany

<sup>e</sup>European Institute for Molecular Imaging, University of Münster, Münster, Germany

## Abstract

In this article we study the potential of the MCP-PMT read-out to detect single photo-electron using transmission lines. Such a solution limits the number of read-out channels, has a uniform time resolution across the PMT surface and provides quasi-continuous measurement of the spatial coordinates. The proposed solution is designed to be used in the BOLD-PET project aiming to develop an innovative detection module for the positron emission tomography using the liquid detection media, the tri-methyl bismuth. In this study we use the commercial MCP-PMT Planacon from Photonis, with 32x32 anode structure. The PCB gathers signals from anode pads in 32 transmission lines which are read-out from both ends. Amplifier boards and SAMPIC modules, developed in our labs, allow us to perform the cost-effective, multi-channel digitization of signals with excellent precision. For a single photo-electron, we measured a time resolution of 70 ps (FWHM) simultaneously with a spatial accuracy of 1.6 mm and 0.9 mm (FWHM) along and across transmission lines correspondingly.

**Keywords:** MCP-PMT, transmission lines, SAMPIC, Planacon

## 1. Introduction

Micro-channel-plate photo multiplier tubes (MCP-PMTs) are position sensitive PMTs which provide the best time resolution up to now. MCP-PMT has quite large surface, typically 60 mm x 60 mm [1–3] and even up to 200 mm x 200 mm [4]. The single photo-electron time transit spread (TTS) is of about 40 ps (SD<sup>1</sup>) [5, 6] In addition, MCP-PMT has a low dark count rate of about 100 Hz/cm<sup>2</sup> (depending on photocathode technology), which makes it an excellent choice for detecting the Cherenkov radiation, for example, in particle physics experiments [5, 7–11]. In order to allow an accurate coordinate resolution, the PMT anode is often structured in 32 x 32 or 64 x 64 pads, providing a resolution of the order of 1 mm and better. The large number of anodes requires a large number of electronics channels if read-out individually. To reduce the number of channels a read-out scheme based on delay lines is used. Most of these configurations are optimized for obtaining a high coordinate resolution, see e.g. [12, 13], but in the project BOLD-PET we need to achieve simultaneously a high time resolution.

The BOLD-PET projects aims to develop an innovative detection module for precise positron emission tomography (PET) imaging. The detection module uses a heavy

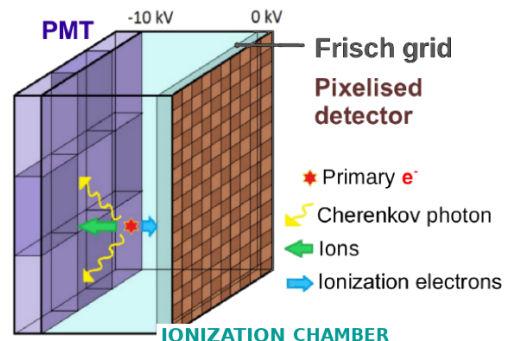


Figure 1: Principle scheme of the BOLD-PET detector. The primary electron created by 511-keV  $\gamma$  produces Cherenkov light and ionizes the medium.

liquid media, tri-methyl bismuth (TMBi), which has a short, 25 mm, attenuation length and high, 47%, photoelectric fraction for converting the 511 keV photon to a relativistic electron. This electron produces Cherenkov radiation and ionizes the medium. The detector operates as a time-projection chamber and detects both light and charge signals, see Fig. 1 and [14, 15]. Ionization signal is read-out in a classical Frisch grid configuration using densely pixelated anode matrix and is used to determine precisely the 2D position of the gamma interaction. The optical photons provide a precise timing to determine the 3D coordinate using the ionization drift time and to improve the

\*Corresponding author

Email address: viatcheslav.sharyy@cea.fr (V. Sharyy)

<sup>1</sup>Standard Deviation

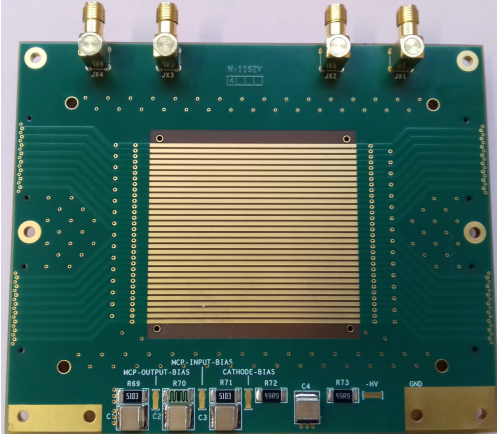


Figure 2: Transmission lines PCB.

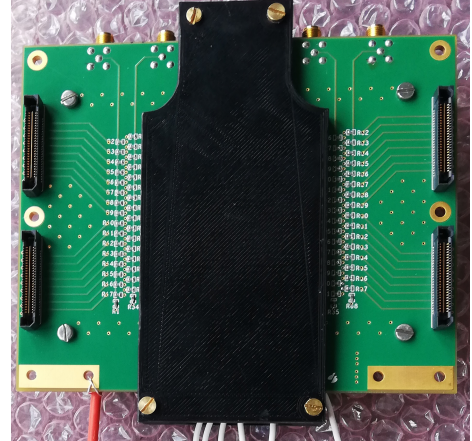


Figure 3: Transmission line PCB clamping to the PMT with the plastic brace.

quality of the image reconstruction with the time-of-flight technique [16–18]. In this project, the optical photons are detected with a MCP-PMT.

In order to limit the number of the electronics channels but keep high time resolution, we develop a read-out scheme using transmission lines as presented in this publication. This read-out scheme is inspired by the approach developed in [19–22], but has substantial differences in the way we plan to use it. In references [19–22] the PMT is coupled with high yield scintillation crystal (LYSO, LSO), thus a large number of optical photons induce signals on all lines. In such configuration, it is not possible to distinguish signals from individual photons, but rather reconstruct the mean position of the induced signals along and across lines. In our approach, 1 to 2 photo-electrons are generated in average at the photocathode [15]. The main focus of our studies is to optimize the whole system to have the best possible performance for an individual photo-electron signal.

## 2. Readout Realization

To study the feasibility and performance of transmission line read-out we use Photonis MCP-PMT Planacon XP85122 with  $32 \times 32$  anode structure and  $10 \mu\text{m}$  pore diameter [23]. Each row of 32 pads (1.1 mm side, inter-pads distance is 0.5 mm) is connected to a line at the printed circuit board (PCB) and signals induced at the line are read-out from both ends, see Fig. 2.

In order to be able to test different PCBs with the same PMT, we use the pressure-sensitive anisotropic conductive interface to connect transmission line PCB to the anode pads. Such reworkable solution doesn't require soldering and provides a low contact resistance, when sufficient pressure is applied. We tested two types of interfaces: the 3M<sup>TM</sup> adhesive tape [24] and Shin-Etsu MT-type of Inter-Connector<sup>®</sup> sheet [25]. Both solutions give reasonably good contacts under the pressure provided by the plastic or metallic brace, as shown in Fig. 3.

The transmission lines board should ensure an electrical contact of matched impedance between the PMT anodes and amplifiers. We have chosen a PCB thickness of 3 mm to ensure sufficient rigidity. It is also desirable that the transmission line protrudes from the electronic board, in order to maximize the pressure between contacts. We therefore removed the varnish in the contact area, and used a copper thickness of  $70 \mu\text{m}$  + gold plating, for a total line thickness of  $100 \mu\text{m}$ . The transmission lines were carefully matched to 50 Ohm, up to the connectors. This includes an impedance calculation of the necessary vias, and careful implementation of ground planes. We placed the MCP-PMT high voltage bias circuit (3 kV) on this board with a low pass filter at the input to damp noises from the power supplies. Finally, we made sure that the line length were as homogeneous as possible, in order to avoid excessive delays in the readout of the signals.

The signals from both ends are amplified by 64 amplifiers, mounted on a PCB which is directly plugged to the transmission line PCB (TL board) through high density SAMTEC connectors QRM8/QRF8 [26], Fig. 4. The typical rise time of this PMT pulse is measured to be 450 ps (10%–90%), so we decided to limit the bandwidth of the amplification stages to 700 MHz to smooth slightly the signal. For a 6.4 GSPS sampling rate of SAMPIC, this allows to capture three samples on the leading edge and avoid thus the undersampling effect that could degrade the time calculation. The single photo-electron signals at the output of MCP-PMT are a few mV. A gain of 100 is therefore appropriate for the 1200 mV range of the SAMPICs input. The integration of the 64 amplifier channels on an area close to that of the PMT imposes severe integration constraints and also requires to control thermal dissipation and crosstalk phenomena between channels to ensure the stability and reliability of the boards. Two amplification stages were necessary for the required performance and to fully meet the specifications. Each card, providing an amplification stage, dissipates 6W for 64 amplifier

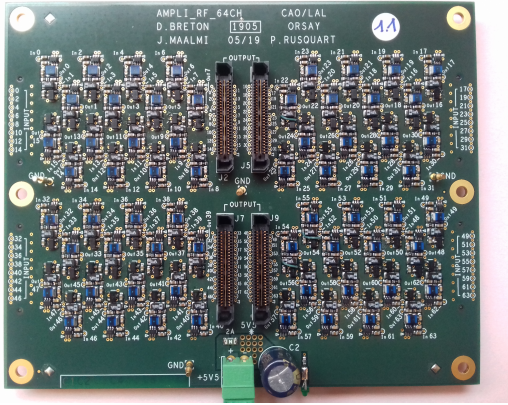


Figure 4: Amplification board.

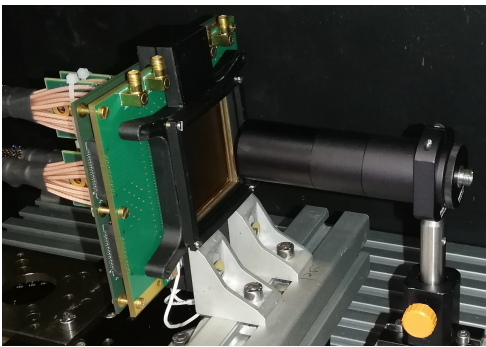


Figure 5: PMT with the readout system, mounted in the black box.

channels, a very low value in this frequency range. In this study, the first amplification stage is mounted directly on the PMT board, and the output signals from the amplifiers are transmitted through the 50 Ohm cables to the second amplification stage outside of the black box. The PMT, assembled with the TL board and 1st stage amplification board, is shown in Fig. 5.

Finally, all signals are digitized by the 64-channel SAMPIC module [27–30], which uses four 16-channel SAMPIC\_V3C chips, based on the patented concept of waveform and time-to-digital converter, Fig. 6. Each channel of the chip includes a delay-locked loop based TDC to provide a rough time associated with an ultra-fast analog memory. The signal sampling frequency can be varied from 1.6 to 8.5 GS/s (6.4 GS/s frequency is adopted in this work). The acquired waveforms are used for the precise timing measurement on-line, but also can be stored for the off-line processing. In this study, we are using a constant fraction discriminator algorithm (CFD) to estimate the time of a signal with the threshold of  $0.5 \times$  amplitude. This module allows to reach a timing accuracy of about 5 ps (SD) between channels from one chip, and slightly larger values between different chips [31]. Every channel integrates a discriminator that can trigger independently. A first trigger level is implemented on-chip, while a chip-related logic is realized at the module level using 4 inputs from 4 chips.

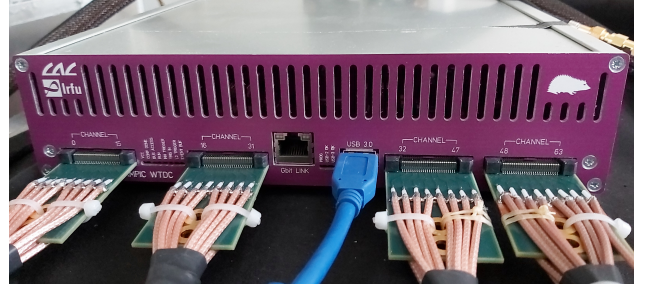


Figure 6: 64-channel SAMPIC module.

### 3. Time and Spatial Resolution

We test the designed system by scanning the surface of the PMT with the optical photons emitted by a pulsed laser as described below. The results of the scan allow us to measure a PMT transit time spread (TTS) at different positions and investigate the spatial resolution of the individual photon reconstruction. Indeed, a difference in signal time from the left and right ends of the line allows to reconstruct the coordinate along the line (x-coordinate). The sum of left and right signal times measures the detection time of a photon. The coordinate across lines (y-coordinate) is reconstructed as a weighted mean of charge, integrated on each line.

#### 3.1. Measurement

For the measurement we use the pulsed laser Pilas by A.L.S. [32] as a light source. The laser beam has a Gaussian-like time profile with duration of about 20 ps (FWHM<sup>2</sup>) and a jitter of 1.4 ps [32]. The light beam from the laser fiber is collimated by a pin-hole of 100  $\mu\text{m}$  diameter. The system of the laser fiber and pin hole is mounted at two-axis X-Z motion system, assembled from two X-LRT0100AL-C linear stages from Zaber Technologies Inc. This system allows to move and position the light source with a precision better than 25  $\mu\text{m}$  [33].

The distance between laser output and pin-hole is about 100 mm and between pin-hole and PMT window is about 20 mm, resulting in a light spot of diameter 120  $\mu\text{m}$ . We choose distances and the light intensity in such way that the PMT is working in a single-photon regime with a detection efficiency of 2% corresponding to a ratio of two-photons / single-photon events of 1%. This number is sufficiently small, that in the following studies we ignore the presence of events with two photons. We realized a detector scan with step of 2 mm along the lines and 0.2 mm across the lines. The data taking time of 1.5 s in each position allows to accumulate of about 3000 events per position. For each signal we register amplitude and CFD signal time for all channels in coincidence with the laser trigger. We use the so-called “L2 coincidence” option of

<sup>2</sup>FWHM: Full Width at Half Maximum. FWTM: Full Width at Tenth of Maximum

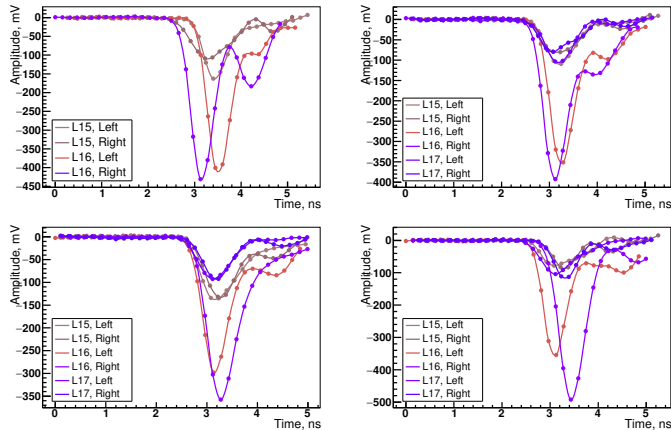


Figure 7: Typical signals registered for positions (from left to right):  $(x, \text{mm}; y, \text{mm}) = (29.0, 65.2) (41.0, 65.2) (53.0, 65.2) (65.0, 65.2)$

the SAMPIC module, with a 30 ns coincidence time window. The threshold value for accepting signals is 50 mV (a typical signal amplitude is about 300 – 400 mV).

### 3.2. Time Resolution

The typical signals are shown in Fig. 7 for different position along the same line. As one can see, typically 2-3 lines are responding to the electron avalanche produced by the photon. The reason for this is that during the propagation between the MCP and the anode plane, an electron avalanche produces a signal on the surface of a few millimeters in size. The largest amount of charge is induced on the closest line and, typically, 3 times lower charge is induced on the neighboring lines. The irregularity in the contact between transmission lines PCB and anode may lead to an increased contact resistance between pads and the line and so redistributes more charge to neighboring lines.

To determine the time of arrival of a photon (PMT time), we choose the line with the highest amplitude and sum up signal time measured at the left and right ends of the line. The difference between the PMT time and laser trigger time is shown in Fig. 8. We decided to fit this spectrum with a triple Gaussian formula:

$$f(t) = \frac{n}{\sqrt{2\pi}} \left( \frac{1 - f_1 - f_2}{\sigma_1} e^{-\frac{1}{2} \left( \frac{t-t_1}{\sigma_1} \right)^2} + \frac{f_1}{\sigma_2} e^{-\frac{1}{2} \left( \frac{t-t_1-t_2}{\sigma_2} \right)^2} + \frac{f_2}{\sigma_3} e^{-\frac{1}{2} \left( \frac{t-t_1-t_3}{\sigma_3} \right)^2} \right), \quad (1)$$

where  $n$  is a normalization coefficient,  $f_1$ ,  $f_2$  are fractions of events in second and third Gaussian terms,  $t_1$  is the mean of the first term,  $t_2$ ,  $t_3$  are the additional delays for the second and third terms,  $\sigma_1$ ,  $\sigma_2$ ,  $\sigma_3$  are the corresponding standard deviations. We fit the spectrum in the range of  $[-0.5 \text{ ns}, 2.5 \text{ ns}]$ .

As one can see about 75% of events have gaussian-like distribution with the width of about 67 ps (FWHM)

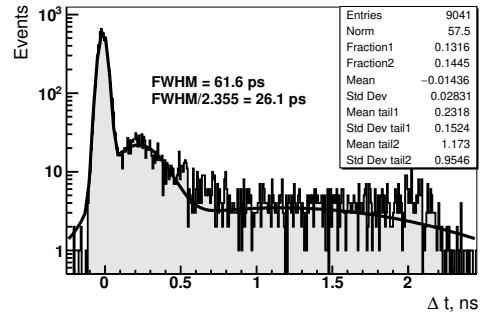


Figure 8: Difference in time between PMT and laser trigger signal for position  $(x, \text{mm}; y, \text{mm}) = (53, 66)$ . Statistical box shows the fit results with function (1). The FWHM is calculated by interpolation between neighboring bin values.

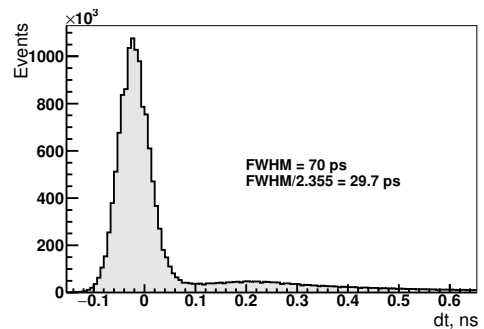


Figure 9: Difference in time between PMT and laser trigger signal averaged over whole PMT surface. The FWHM is calculated by interpolation between neighboring bin values.

and the other 25% corresponds to the back-scattered electrons [34, 35] and form a long tail. Such fit is done in each position and Fig. 9 shows the value averaged over whole PMT surface. The obtained value 70 ps (FWHM) is larger than the simple average in all positions, 65 ps, due to the residual imperfections in calibration. Fig. 10 and 11 show the width of the distribution as well as the fraction of electrons delayed for more than 100 ps as a function of  $x$  and  $y$ -coordinates.

### 3.3. Spatial Resolution

To reconstruct the coordinate across lines ( $y_R$ ), we choose the line with the largest amplitude and calculate the weighted average of coordinates for this line and the two closest neighbors:

$$y_R = \frac{\sum_{i=1}^3 y_i C_i}{\sum_{i=1}^3 C_i}, \quad (2)$$

where  $y_i$  is a  $y$ -coordinate of the center of line  $i$ ,  $C_i$  is a charge at the same line, measured as a sum of signals over all 64 sampling points. Fig. 12 shows the resolution of the reconstructed  $y$ -coordinate as a function of the linear stage's  $x$ - and  $y$ -coordinates and Fig. 14 shows the difference between reconstructed and linear stage's  $y$ -coordinates for all registered positions. In average, the

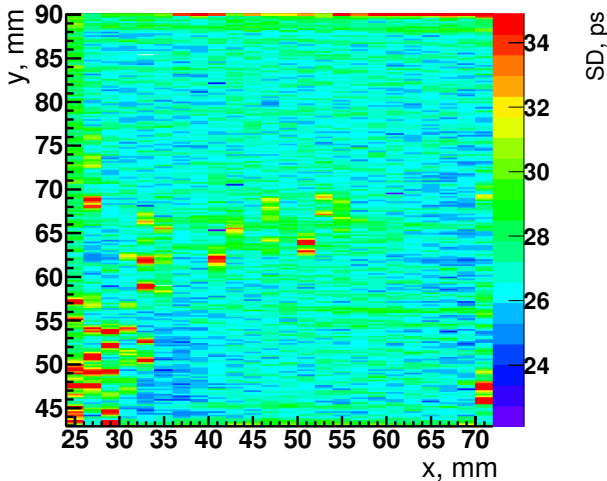


Figure 10: Width (SD) of the time distribution (parameter  $\sigma_1$  in the function (1)).

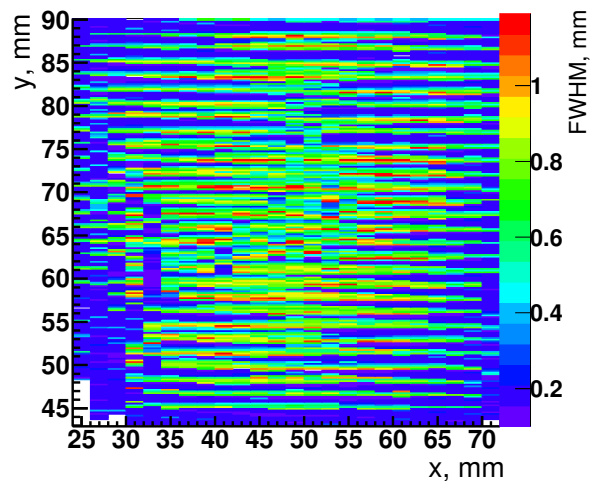


Figure 12: Resolution of the reconstructed y-coordinate (across lines, FWHM) as a function of linear stage's x- and y-coordinates.

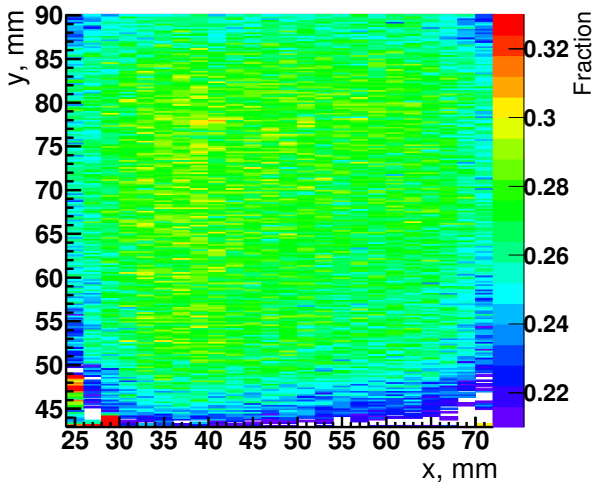


Figure 11: Fraction of events delayed more than 100 ps relatively to the position of the main peak.

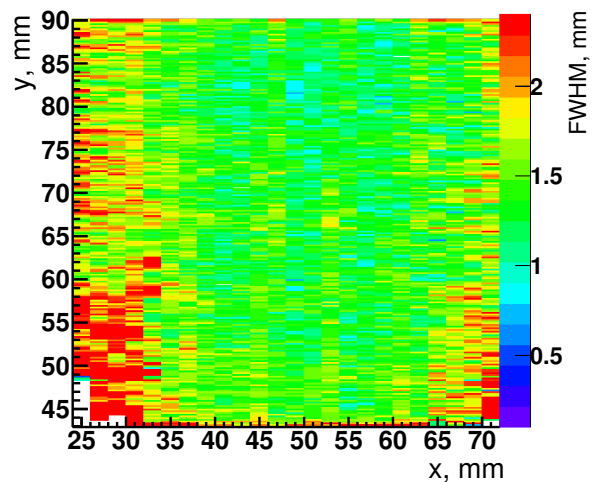


Figure 13: Resolution of the reconstructed x-coordinate (along lines, FWHM) as a function of linear stage's x- and y-coordinates.

resolution of about 0.9 mm is achieved with a variation between 0.3 and 1.2 mm depending on the position.

The coordinate along lines ( $x_R$ ) is reconstructed as  $x_R = (t_R - t_L)s$ , where  $t_R$  and  $t_L$  is a time measured at the right and left line extreme respectively and  $s$  is a signal propagation speed, measured to be about 0.36 x speed-of-light. Fig. 13 and 15 show the resolution distributions for the x-coordinate. We obtain a precision of about 1.6 mm (FWHM) in average with the variation between 0.8 and 2.5 mm. The resolution in x depends on the precision in the signal time evaluation at both ends of the line. In order to estimate the expected precision, we developed a simulation, which uses the measured shape of the signal, simulates the digitization of signals with the step 156.25 ps, applies the randomized white noise to the digitized shape. Fig. 16 shows the estimated time resolution calculated for the different levels of the electronics noise. The noise in the experiment is measured using sig-

nal baseline and includes all electronics contribution, e.g. noise during amplification, propagation in cables, digitization by the SAMPIC module. As shown, in Fig. 17 the typical value is about 1 mV and hence the expected spatial resolution along the line should be below 1 mm according to the simulation. The lowest value observed in the measurement corresponds roughly to the value in the simulation. The average resolution value of 1.6 mm is significantly larger due to effects not accounted for in the simulation, e.g. signal shape deformation during the propagation over the transmission lines, fluctuation in the signal shape and amplitude related to the uniformity of the PCB, non-uniformity of the electrical contacts between PCB and pads, border effects, imperfection in calibration functions etc.

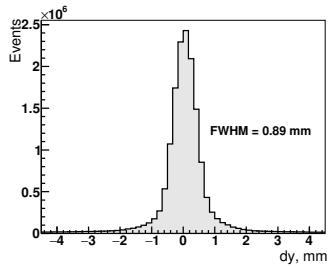


Figure 14: Difference between reconstructed and linear stage's y-coordinates for all positions.

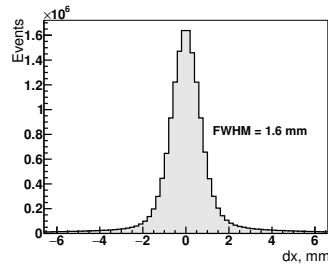


Figure 15: Difference between reconstructed and linear stage's x-coordinates for all positions.

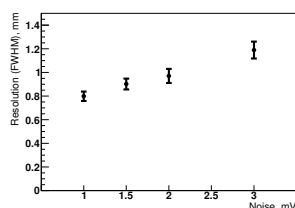


Figure 16: Resolution of the x-coordinate reconstruction estimated by the simulation as a function of the electronic noise level.

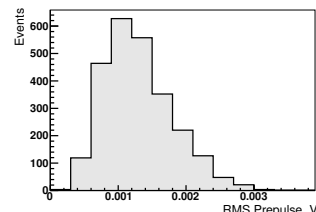


Figure 17: Typical noise distribution for a single position, measured as the RMS of the signal baseline samples.

### 3.4. Discussion

Results presented in the previous sections demonstrate that one can reconstruct a single-dielectron coordinate along and across the readout line with a precision of 1.6 mm and 0.9 mm simultaneously with the time resolution of about 70 ps. This time resolution is limited mainly by the PMT TTS with a small contribution due to imperfections in the calibration. For the simultaneous detection of two and more photons the situation will be quite different.

Registered photo-electrons separated by at least two lines, will be reconstructed independently and with the same precision. On the contrary, if photo-electrons are happened to be on the same line, it will lead to the overlap between the induced signals and to a deformation of the signal shape. In the BOLD-PET projects, we expect to detect in average 1 – 2 optical photons per event [15]. The probability that those two photons will cause the signal overlap is quite low, and hence such events could be rejected.

Such read-out can be and is planned to be used in the situation with a larger number of detected photo-electrons. For example, we plan to use similar read-out scheme in the ClearMind project [36], where the expected number of photo-electrons per event is about twenty. Depending on the depth-of-interaction of the gamma conversion, the detected events may contain more or less overlapping signals. In such situation, more complicated reconstruction algorithms and, in particular, algorithms based on the machine learning approach, allow to mitigate the overlap and reconstruct the gamma-conversion coordinates with a millimetric precision without degrading the time resolution.

## 4. Conclusion

In this study we demonstrate the possibility to read-out the MCP-PMT with transmission lines and obtain simultaneously an excellent time resolution on whole surface of the PMT and good spatial resolution. The obtained values fully satisfy requirements to the optical read-out in the BOLD-PET project and will be used there to detect the Cherenkov light, generated by the conversion of the 511 keV gamma in the liquid TMBi radiator.

The use of amplifier boards and SAMPIC module, developed in our labs, allow us to realize the cost-effective, multi-channel digitization of signals with excellent precision. For a single photo-electron, we obtain the average time resolution of 70 ps (FWHM), and coordinates resolution of 1.6 mm and 0.9 mm (FWHM) along and across the line respectively.

## Acknowledgments

We thank professor Henry Frisch from the University of Chicago for the fruitful discussion on the readout PCB technology and for providing us a transmission lines read-out board [19], which was used for first tests in our development. We thank Irakli Mandjavidze from IRFU, CEA for his studies and advises on optimizing signal propagation through transmission lines.

We acknowledge the financial support by the joint French-German grants ANR-18-CE92-0012-01, DFG-SCHA 1447/3-1 and WE 1843/8-1. This work is conducted in the scope of the IDEATE International Associated Laboratory (LIA).

## References

- [1] Photonis, Planacon MCP-PMT [cited July 13, 2021]. URL <https://www.photonis.com/products/planacon>
- [2] Hamamatsu, Micro-Channel-Plate PMT [cited July 1st, 221]. URL [https://www.hamamatsu.com/eu/en/product/optical-sensors/pmt/pmt\\_tube-alone/mcp-pmt/index.html](https://www.hamamatsu.com/eu/en/product/optical-sensors/pmt/pmt_tube-alone/mcp-pmt/index.html)
- [3] Photek, Auratek-MAPMT253 Datasheet [cited July 1st, 221]. URL <http://www.photek.com/pdf/datasheets/detectors/DS034-Auratek-MAPMT253-Detector-Datasheet.pdf>
- [4] M. J. Minot, B. W. Adams, M. Aviles, J. L. Bond, T. Cremer, M. R. Foley, A. Lyashenko, M. A. Popecki, M. E. Stochaj, W. A. Worstell, M. J. Wetstein, J. W. Elam, A. U. Mane, O. H. W. Siegmund, C. Ertley, H. J. Frisch, A. Elagin, E. Angelico, E. Spieglan, Large Area Picosecond Photodetector (LAPPDTM) - Pilot production and development status, Nucl. Instrum. Meth. A 936 527–531. doi:10.1016/j.nima.2018.11.137.
- [5] J. Va`vra, Journal of physics: Conference series 1498 (1) 012013. doi:10.1088/1742-6596/1498/1/012013.
- [6] C. Canot, M. Alokhina, P. Abbon, J. P. Bard, D. Breton, E. Delagnes, J. Maalmi, G. Tauzin, D. Yvon, V. Sharyy, Fast and efficient detection of 511 keV photons using Cherenkov light in PbF2 crystal, coupled to a MCP-PMT and SAMPIC digitization module, J. Instrum. 14 (12) (2019) P12001–P12001. doi:10.1088/1748-0221/14/12/p12001.
- [7] F. Davi, W. Erni, B. Krusche, M. Steinacher, N. Walford, H. Liu, Z. Liu, B. Liu, X. Shen, C. Wang, J. Zhao, M. Albrecht, T. Erlen, F. Feldbauer, M. Fink, V. Freudenreich, M. Fritsch, F. H. Heinsius, T. Held, T. Holtmann, I. Keshk, H. Koch, B. Kopf, M. Kuhlmann, M. Kümmel, S. Leiber,

- P. Musiol, A. Mustafa, M. Pelizáus, A. Pitka, G. Reicherz, M. Richter, C. Schnier, T. Schröder, S. Sersin, L. Sohl, C. Sowa, M. Steinke, T. Triffterer, U. Wiedner, R. Beck, C. Hammann, J. Hartmann, B. Ketzer, M. Kube, M. Rossbach, C. Schmidt, R. Schmitz, U. Thoma, M. Urban, A. Bianconi, M. Bragadireanu, D. Pantea, W. Czyzycki, M. Domagala, G. Filo, J. Jaworowski, M. Krawczyk, E. Lisowski, F. Lisowski, M. Michalek, J. Plazek, K. Korcyl, A. Kozela, P. Kulesa, P. Lebedowicz, K. Pysz, W. Schäfer, A. Szczurek, T. Fiutowski, M. Idzik, B. Mindur, K. Swientek, J. Biernat, B. Kamys, S. Kistryn, G. Korcyl, W. Krzemien, A. Magiera, P. Moskal, W. Przygoda, Z. Rudy, P. Salabura, J. Smyrski, P. Strzemppek, A. Wronska, I. Augustin, R. Böhm, I. Lehmann, D. N. Marinescu, L. Schmitt, V. Varentsov, M. Al-Turany, A. Belias, H. Deppe, N. D. Veis, R. Dzhygadlo, H. Flemming, A. Gerhardt, Technical Design Report for the PANDA Endcap Disc DIRC, arXiv (Dec 2019). arXiv:1912.12638.  
URL <https://arxiv.org/abs/1912.12638>
- [8] N. H. Brook, L. C. García, T. M. Conneely, D. Cussans, M. W. U. van Dijk, K. Föhl, R. Forty, C. Frei, R. Gao, T. Gys, T. H. Hancock, N. Harnew, J. Lapington, J. Milnes, D. Piedigrossi, J. Rademacker, A. R. García, Testbeam studies of a TORCH prototype detector, Nucl. Instrum. Meth. A 908 (2018) 256–268. doi:10.1016/j.nima.2018.07.023.
- [9] V. A. Grigoryev, V. A. Kaplin, T. L. Karavicheva, A. B. Kurepin, E. F. Maklyaev, Y. A. Melikyan, D. V. Serebryakov, W. H. Trzaska, E. M. Tykmanov, Study of the Planacon XP85012 photomultiplier characteristics for its use in a Cherenkov detector, J. Phys. Conf. Ser. 675 (4) (2016) 042016. doi:10.1088/1742-6596/675/4/042016.
- [10] W. H. Trzaska, New Fast Interaction Trigger for {ALICE}, Nucl. Instrum. Meth. A (2016) –doi:10.1016/j.nima.2016.06.029.
- [11] S. Hirose, T. Iijima, K. Inami, D. Furumura, T. Hayakawa, Y. Kato, K. Matsuoka, R. Mizuno, Y. Sato, K. Suzuki, T. Yonekura, Development of the micro-channel plate photomultiplier for the Belle II time-of-propagation counter, Nucl. Instrum. Meth. A 787 (2015) 293–296. doi:10.1016/j.nima.2014.12.082.
- [12] O. H. W. Siegmund, M. A. Gummin, J. M. Stock, D. R. Marsh, R. Raffanti, J. S. Hull, High-resolution monolithic delay-line readout techniques for two-dimensional microchannel plate detectors, in: EUV, X-Ray, and Gamma-Ray Instrumentation for Astronomy IV, Vol. 2006, International Society for Optics and Photonics, pp. 176–187. doi:10.1117/12.162851.
- [13] J. G. Timothy, Microchannel plates for photon detection and imaging in space, in: Observing Photons in Space, ISSI Scientific Report Series, Springer, New York, NY, 2013, pp. 391–421. doi:10.1007/978-1-4614-7804-1\_22.
- [14] D. Yvon, J.-P. Renault, G. Tauzin, P. Verrecchia, C. Flouzat, S. Sharyy, E. Ramos, J.-P. Bard, Y. Bulbul, J.-P. Mols, P. Starzynski, D. Desforge, A. Marcel, J.-M. Reymond, S. Jan, C. Comtat, R. Trebossen, CaLIPSO: An Novel Detector Concept for PET Imaging., IEEE Transactions on Nuclear Science 61 (1) (2014) 60 – 66. doi:10.1109/TNS.2013.2291971.
- [15] E. Ramos, D. Yvon, P. Verrecchia, G. Tauzin, D. Desforge, V. Reithinger, D. Dubreuil, M. Hamel, C. Flouzat, V. Sharyy, J. P. Bard, Y. Bulbul, J. P. Mols, P. Starzynski, A. Marcel, R. Granelli, Trimethyl Bismuth Optical Properties for Particle Detection and the CaLIPSO Detector, IEEE Transactions on Nuclear Science 62 (3) (2015) 1326–1335. doi:10.1109/TNS.2015.2424080.
- [16] S. Vandenberghe, E. Mikhaylova, E. D’Hoe, P. Mollet, J. S. Karp, Recent developments in time-of-flight PET, EJNMMI Physics 3 (1) (2016). doi:10.1186/s40658-016-0138-3.
- [17] P. Lecoq, C. Morel, J. O. Prior, D. Visvikis, S. Gundacker, E. Auffray, P. Krizan, R. M. Turtos, D. Thers, E. Charbon, J. Varela, C. de La Taille, A. Rivetti, D. Breton, J.-F. Pratte, J. Nuyts, S. Surti, S. Vandenberghe, P. Marsden, K. Parodi, J. M. Benlloch, M. Benoit, Roadmap toward the 10 ps time-of-flight PET challenge, Physics in Medicine & Biology 65 (21) (2020) 21RM01. doi:10.1088/1361-6560/ab9500.
- [18] D. R. Schaart, Physics in medicine and biology arXiv:33711831, doi:10.1088/1361-6560/ab9500.
- [19] H. Kim, C.-T. Chen, H. Frisch, F. Tang, C.-M. Kao, A Prototype TOF PET Detector Module Using a Micro-Channel Plate Photomultiplier Tube with Waveform Sampling, Nucl. Instrum. Meth. A 662 (1) (2012) 26–32. doi:10.1016/j.nima.2011.09.059.
- [20] H. Grabas, R. Obaid, E. Oberla, H. Frisch, J.-F. Genat, R. Northrop, F. Tang, D. McGinnis, B. Adams, M. Wetstein, RF strip-line anodes for psec large-area MCP-based photodetectors, Nucl. Instrum. Meth. A 711 (2013) 124–131. doi:10.1016/j.nima.2013.01.055.
- [21] H. Kim, C. T. Chen, N. Eclou, A. Ronzhin, P. Murat, E. Ramberg, S. Los, C. M. Kao, A silicon photo-multiplier signal read-out using strip-line and waveform sampling for Positron Emission Tomography, Nucl. Instrum. Meth. A 830 (2016) 119–129. doi:10.1016/j.nima.2016.05.085.
- [22] E. Angelico, T. Seiss, B. Adams, A. Elagin, H. Frisch, E. Spieglan, Capacitively coupled pickup in MCP-based photodetectors using a conductive metallic anode, Nucl. Instrum. Meth. A 846 (2017) 75–80. doi:10.1016/j.nima.2016.12.008.
- [23] Photonis, XP85122 Datasheet, Tech. rep. (2014).  
URL <https://www.photonis.com/products/planacon>
- [24] 3M, Electrically Conductive Adhesive Transfer Tape 9703.  
URL [https://www.3m.com/3M/en\\_US/p/d/b10167835/](https://www.3m.com/3M/en_US/p/d/b10167835/)
- [25] Shin-Etsu Polymer, Inter-Connector<sup>®</sup> MT-type [cited July 13, 2021].  
URL <https://www.shinetsu.info/product/mt-type-of-inter-connector>
- [26] SAMTEC, Q-Rate Connectors (2021) [cited July 1st, 221].  
URL <https://www.samtec.com/>
- [27] E. Delagnes, H. Grabas, D. Breton, J. Maalmi, The sampic WTDC chip, Workshop on Picosecond Photon Sensors for physics and medical application (March 2014).
- [28] D. Breton, Measuring time with a 5-ps precision at the systel level with the WaveCatcher family of SCA-based fast digitizers, in: Workshop in picosecond photon sensors for physics and medical application, March 2014.  
URL <https://indico.cern.ch/event/306859/session/3/contribution/9/material/slides/1.pdf>
- [29] E. Delagnes, D. Breton, H. Grabas, J. Maalmi, P. Rusquart, Reaching a few picosecond timing precision with the 16-channel digitizer and timestamper SAMPIC ASIC, Nucl. Instrum. Meth. A 787 (2015) 245–249. doi:10.1016/j.nima.2014.12.042.
- [30] D. Breton, C. Cheikali, E. Delagnes, J. Maalmi, P. Rusquart, P. Vallerand, Fast electronics for particle Time-Of-Flight measurement, with focus on the SAMPIC ASIC, Nuovo Cimento C 43 (1) 7. doi:10.1393/ncc/i2020-20007-6.
- [31] D. Breton, V. De Cacqueray, E. Delagnes, H. Grabas, J. Maalmi, N. Minafra, C. Royon, M. Saimpert, Measurements of timing resolution of ultra-fast silicon detectors with the SAMPIC waveform digitizer, Nucl. Instrum. Meth. A 835 (Supplement C) (2016) 51–60. doi:10.1016/j.nima.2016.08.019.
- [32] Advanced Laser Diode System A.L.S. GmbH, Picosecond Diode Laser - Pilas, Manual and Test Report CEA PiL040XSM-1.825, Tech. rep. (2017).
- [33] Zaber Technologies Inc., X-LRT-C Series User’s Manual, Tech. rep. (2017).  
URL <https://www.zaber.com/manuals/X-LRT-C>
- [34] S. Korpar, P. Krizan, R. Pestotnik, A. Stanovnik, Timing and cross-talk properties of BURLE multi-channel MCP PMTs, Nucl. Instrum. Meth. A 595 (1) (2008) 169–172. doi:10.1016/j.nima.2008.07.022.
- [35] M. Lipka, M. Parniak, W. Wasilewski, Microchannel plate cross-talk mitigation for spatial autocorrelation measurements, arXiv:1805.04106 [physics] arXiv: 1805.04106 (2018).  
URL <http://arxiv.org/abs/1805.04106>
- [36] D. Yvon, V. Sharyy, M. Follin, J.-P. Bard, D. Breton, J. Maalmi, C. Morel, E. Delagnes, Design study of a “scinronic” crystal targeting tens of picoseconds time resolution for gamma ray

imaging: the ClearMind detector, J. Instrum. 15 (07) (2020)  
P07029. doi:10.1088/1748-0221/15/07/P07029.